

Tuning the magnetic properties of Perpendicular Magnetic Anisotropy stacks

Adrián Gudín Holgado

Máster en Nanociencia
y Nanotecnología Molecular



MÁSTERES
DE LA UAM
2017 - 2018

Facultad de Ciencias

Máster en Nanociencia y Nanotecnología Molecular

Tuning the magnetic properties of Perpendicular Magnetic Anisotropy stacks

Adrián Gudín Holgado

Contents

Abstract.....	2
1. Introduction	3
1.1. Spin-Orbitronics	3
1.2. Spin-Orbit Interaction (SOI)	4
1.3. Magnetic Anisotropy	5
1.3.1 Perpendicular Magnetic Anisotropy (PMA)	5
1.4. Domains and domain walls.....	6
1.5. Exchange energy.....	7
1.6. Magnetization process.....	9
2. Experimental techniques.....	10
2.1. The growth chambers	10
2.1.1 Sputtering chamber	11
2.2. Vectorial-Kerr magnetometry.....	12
2.3. KERR Microscopy	14
3. Results	16
3.1. Growth process.....	16
3.2. Structures a) Pt (t_{Pt} -wedge) / Co (t_{Co}) / Pt (5nm) and b) Pt (t_{Pt} -wedge) / Co (t_{Co}) / Ta (5nm)	17
3.3. Structure c) Pt (t_{Pt}) / Co (t_{Co} -wedge) / Pt (5nm).....	19
4. Conclusions.....	23
5. Acknowledgements	24
6. References.....	24

Abstract

The actual spintronics technology relies on our ability to create magnetic nanostructures in which the magnetic properties are tuned as function of the desired application. In order to novel devices with improved functionalities, e.g. to achieve larger storage density and faster data processing together with a lower energy consumption than the actual magnetic devices, a novel emerging field of Nanomagnetism, called Spin-Orbitronics, which exploits the coupling between spin, charge and orbital moment of the electrons, is attracting large interest in the scientific community [1].

This master thesis, within the context of Spin-Orbitronics, provides a systematic study on the fabrication and the magnetic characterization of magnetic nanostructures with (defined) Perpendicular Magnetic Anisotropy (PMA), focusing on polycrystalline (multilayered) magnetic stacks, based on ferromagnetic (FM) ultra-thin layer coupled with non-magnetic (NM) materials.

The thesis is organized as following:

In the 1st chapter, an introduction on the physics of the interfacial Spin-Orbit Coupling (SOC), the PMA and Dzyaloshinskii-Moriya interaction (DMI) is given;

In the 2nd chapter, the experimental techniques used are described: *i*) growth of the magnetic structures by means of sputtering and MBE, *ii*) magnetic characterizations performed by Kerr magnetometry and microscopy;

The results of the experiments are presented and discussed in the 3rd chapter.

The conclusions are finally given in the last chapter.

1. Introduction

1.1. Spin-Orbitronics

The presence of large Spin–Orbit Interaction (SOI) at transition metal interfaces enables the emergence of a variety of fascinating phenomena that have been at the forefront of spintronics research in the past 10 years. Spin-Orbitronics exploits such a coupling between spins and orbital moment at interfaces (generally) between a 3d ferromagnetic (FM) and 5d heavy-metal (HM) layers to realize artificial structures with tailored functionalities, for example devices in which the generation or detection of spin polarized currents occur without any magnetic field [2]. Fig. 1 presents a schematic illustration of the relation between the presence of Spin-Orbit Coupling (SOC) at transition metals interfaces and the appearance of new interactions and electronic states, such as Dzyaloshinskii-Moriya interaction (DMI), Rashba-interfaces and topological surface states [3]. These phenomena can be exploited and tailored in order to realize devices that convert spin polarized current to charge and vice-versa, innovative magnetic RAM based on spin-orbit torque, new magnetic memories based on chiral spin textures (like magnetic skyrmions, magnetic Néel or Bloch domain walls) [4].

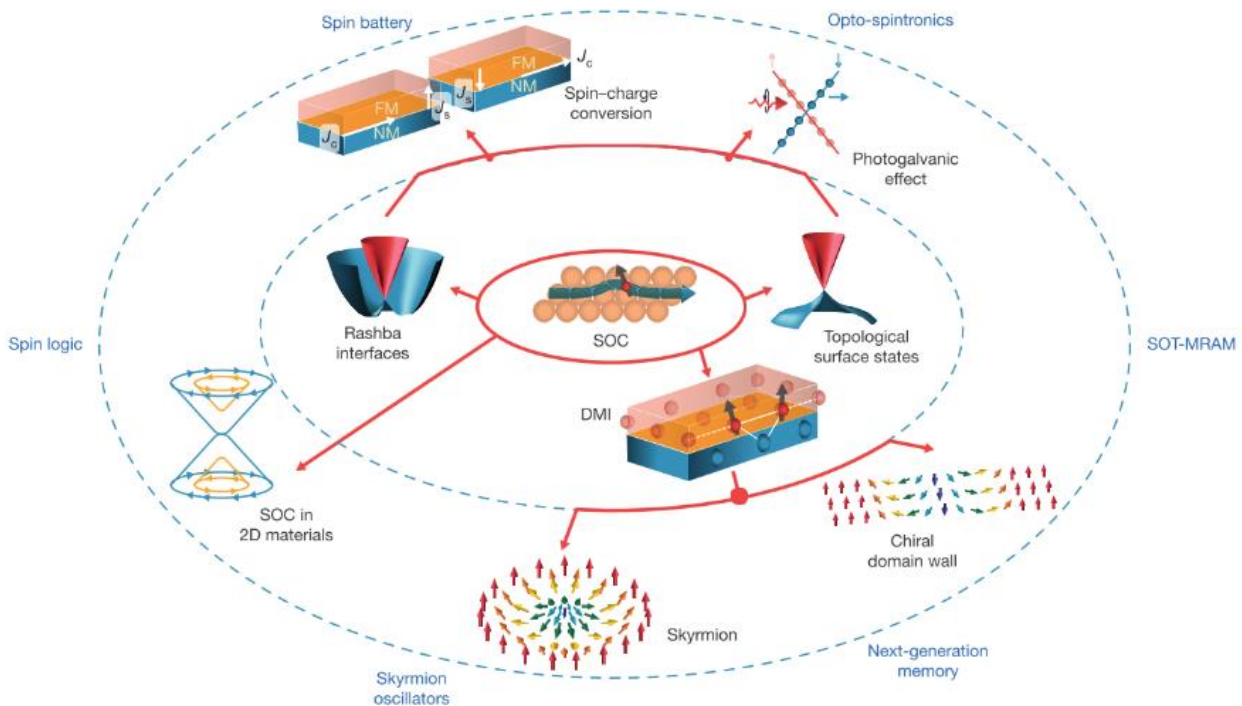


Figure 1.1. Scheme of the emergent phenomena due to spin-orbit coupling (SOC) at interfaces and surfaces (Adapted from [3]).

1.2. Spin-Orbit Interaction (SOI)

In the following, we introduce briefly the physics of SOC. The spin-orbit interaction is a relativistic interaction of a particle's spin with its motion inside a potential. In the classical approximation, the SOI can be expressed as function of the electron induction (\mathbf{B}) created in the system:

$$\hat{H}_{SO} = -\frac{1}{2} \boldsymbol{\mu} \cdot \mathbf{B} \quad (1)$$

Where $\left(\frac{1}{2}\right)$ factor is the relativistic Thomas-Wigner factor, $\boldsymbol{\mu}$ the electron moment being, $\boldsymbol{\mu} = \frac{-e\hbar}{2mc} \boldsymbol{\sigma}$ and $\mathbf{B} = \frac{-\mathbf{v} \times \mathbf{E}}{c}$.

The presence of this effective magnetic field that the electron feels in its relaxed state affects both the dynamics of the spin and the total energy of the electron. To note that the only possible interaction for the spin degree of freedom is with a magnetic field, whose source can be either an externally applied magnetic field, or the effective field generated by the SOI.

Substituting in the equation (1) for the expression of moment of electron ($\boldsymbol{\mu}$) and \mathbf{B} is possible to obtain the following equation:

$$\hat{H}_{SO} = -\frac{Ze^2}{2m_e^2 c^2 r^3} \mathbf{L} \cdot \mathbf{S} \quad (2)$$

which indicates that the electric field experienced by a traveling electron promotes a magnetic field proportional to its velocity, i.e. a relativistic effect which is more notable in crystals with heavy atoms (large Z).

The main feature of any SOC is that, even without an external applied magnetic field, the electrons moving in an electric field experience a magnetic field in their intrinsic motion. The SO field couples to electron's magnetic moment.

1.3. Magnetic Anisotropy

The magnetization vector in a magnetic material generally lies in some preferred directions with respect to the crystalline axes and/or to the external shape of the body. This property is known as magnetic anisotropy, which is defined as the energy that it takes to rotate the magnetization direction from the easy into the hard direction. The magnetic anisotropy is present in magnets of any dimensionality and shape and it is able to stabilize magnetic order in dimensions where the exchange interaction alone would not suffice. The physical origin of the magnetic anisotropy is the asymmetry existing in the overlap of the wave functions: the crystalline structure of the material influences magnetization through SOC [5]. This property determines the direction of magnetization in which the system prefers to be oriented, is termed as easy axis (e.a). While that the direction in which a maximum energy is required to saturate the magnetization is termed as hard axis (h.a). This excess energy required to switch the orientation of the magnetization from e.a to h.a is called as the effective magnetic anisotropy energy (K_{eff}).

In general, two main interactions are responsible for magnetic anisotropies. Dipolar interactions between atomic moments that are related to the shape of a given ferromagnetic object, and SOC that originates the other anisotropies:

- Magneto-elastic anisotropy (e.g., strain induced by the substrate).
- Exchange anisotropy.
- Magneto-crystalline (surface/interface) anisotropy.

1.3.1 Perpendicular Magnetic Anisotropy (PMA)

In 1954, Néel predicted that the reduced symmetry at the surface of the thin films could result in a different anisotropy compared to that of bulk anisotropy [6][7]. Hence, in the case of thin films, the total magneto-crystalline anisotropy energy K_{eff} is given by the contribution of volumetric anisotropy, K_v per unit volume and the contribution from the surface anisotropy, K_s per unit area [6]:

$$K_{eff} = K_v + \frac{K_s}{t} \quad (3)$$

To note that, in the case of ultrathin ferromagnetic layers, the surface anisotropy term affects significantly the total energy. We can define a critical film thickness $t_{crit} = K_s / K_v$ in where the transition change from in plane to out-plane magnetization. This phenomenon is particularly important for applications related to the storage of information, because it opens the possibility of increasing the density of bits per area. Therefore, by varying the film thickness, by choosing the materials composing the interfaces, it is possible to “design” the magnetic anisotropy of the system.

1.4. Domains and domain walls

A magnetic domain defines a region within a magnetic material with uniform magnetization. The regions that separates magnetic domains are termed domain walls, where the magnetization rotates coherently from the direction of one domain to the next. The shape of domains is dictated by the local effective magnetic anisotropy as result of the energy minimization. In fact, if the magnetization were homogeneous in the entire sample, there will need a high cost of magnetostatic energy due to the formation of free poles. To avoid this, the magnetization is divided into domains and arranged in a way to minimize the field energy (as shown in Figure 1.2). The width of the domain wall is strongly dependent on the material and its anisotropies, and is typically of the order of tens to 100 nm.

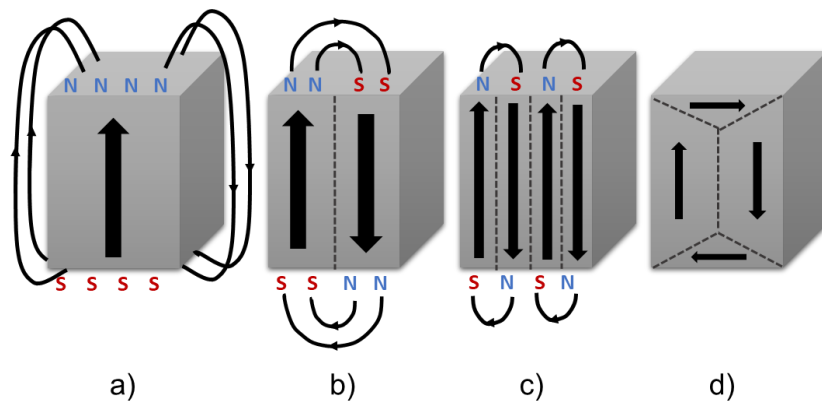


Figure 1.2. Schematic illustration of the breakup of magnetization into domains a) single domain, b) two domains, c) Four domains and d) closure domains [5].

We can find two types of walls between the domains:

- Bloch wall:** the magnetization is contained in a plane perpendicular to the plane of the film, and adds to the energy of the wall a demagnetizing energy proportional to the volume of the wall.
- Néel wall:** the magnetization is parallel to the surface. When the thickness of the film is small compared to the width of the film (ultra-thin-films), the formation of this type of walls is favorable, since its energetic cost is negligible.

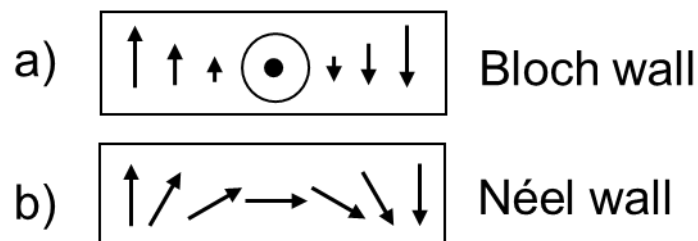


Figure 1.3. Schematic diagrams showing a) Bloch wall, b) Néel wall.

1.5. Exchange energy

In any solid material, the electronic orbitals of neighboring atoms overlap, this produce the correlation of the electrons. The total energy of the crystal depends hence on the relative orientation of spins localized on neighboring atoms. The exchange interaction is responsible for the existence of the parallel, i.e. ferromagnetic, antiparallel, i.e. antiferromagnetic order.

The exchange interactions might be due to different mechanisms depending on the material. The most important mechanisms are Direct exchange and Antisymmetric exchange: Dzyaloshinskii-Moriya interaction [8].

Direct exchange

The direct exchange is due to a direct overlap of electronic wave functions of the neighboring atoms and the Pauli Exclusion Principle, requiring different symmetry properties from the spatial and spin parts of the wave function.

$$H_{ex} = - \sum_{i \neq j} J_{ij} \hat{S}_i \cdot \hat{S}_j \quad (4)$$

Where J_{ij} is the exchange integral describing the coupling between two spins or magnetic moments represented by the spin operator \hat{S}_i and \hat{S}_j . Depending on orbital overlaps (i.e. the interatomic distances) the values of J_{ij} might have a positive or negative sign, resulting in the parallel or antiparallel ground state configuration of spins, respectively.

Antisymmetric exchange: Dzyaloshinskii-Moriya interaction (DMI)

This exchange gives rise from SOC in systems with that lack inversion symmetry (systems where inversion symmetry is broken, e.g. by the presence of an interface). The DMI can be mathematically expressed by [4][8]:

$$H_{DMI} = -(\mathbf{S}_1 \times \mathbf{S}_2) \cdot \mathbf{D}_{12} \quad (5)$$

Where \mathbf{S}_1 and \mathbf{S}_2 are neighboring spins and \mathbf{D}_{12} is the Dzyaloshinskii-Moriya vector. The DMI is thus a chiral interaction that increases or decreases the energy of the spins depending on whether the rotation from \mathbf{S}_1 to \mathbf{S}_2 around \mathbf{D}_{12} is anticlockwise or clockwise. As illustrated in Fig. 1.5 \mathbf{D}_{12} emerges in a plane, parallel to the surface, pointing outer from the plane of the spins.

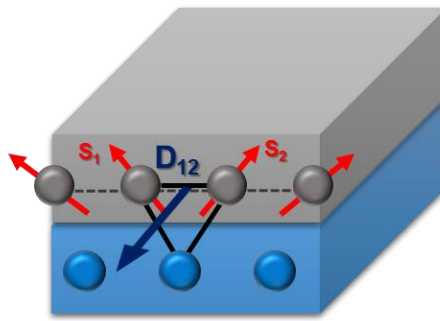


Figure 1.4. Dzyaloshinskii-Moriya Interaction for a system composed of a magnetic layer (grey) and heavy metal (blue).

High processing speed and high density data storage with reduced energy consumption can be achieved by exploiting chiral Néel-type magnetic domain walls (DWs) and magnetic skyrmions as carriers of digital information [4]. It has been demonstrated that in non-centrosymmetric multilayer stacks with PMA, the presence of the antisymmetric DMI favors a chiral arrangement of spins within the domain walls (DWs) [4][9]. Such DMI stabilizes also magnetic skyrmions, i.e. the topologically protected, nanometer-sized, whirling magnetic objects which have been observed in the presence of strong magnetic fields and at low temperature and recently detected at RT under low or vanishing magnetic fields [9][11]. By balancing the uniaxial PMA and the DMI by acting on the nature and thickness of the materials composing the stacks, one can tune the stability and the dimension of the chiral Néel DWs [10]. In particular, the DMI strength can be tuned by using two-active interfaces [12][13] as schematically shown in Fig. 1.5.

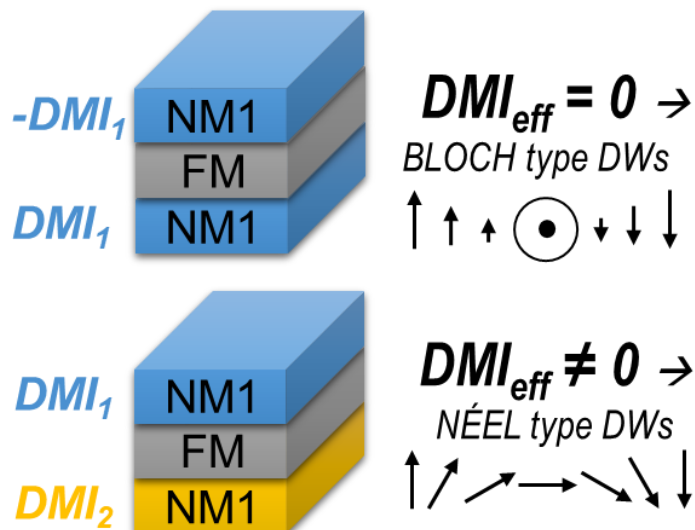


Figure 1.5. Schematic illustration of symmetric and antisymmetric stack with corresponding effective DMI.

1.6. Magnetization process

The field driven magnetization reversal in a ferromagnetic material is a gradual process that usually begins with the nucleation of some domains (normally at low coordination sites: lattice defects, grain boundaries, ..) aligned with the external field and further domain walls propagation. By looking at the hysteresis loop in Fig. 1.6, we can define the most relevant points during a magnetization vs. magnetic field loop: "magnetization saturation" M_s , that is maximum value reached by the magnetization; "remanence magnetization" M_r , i.e. magnetization at zero field; coercive field H_c , value of the field at zero magnetization.

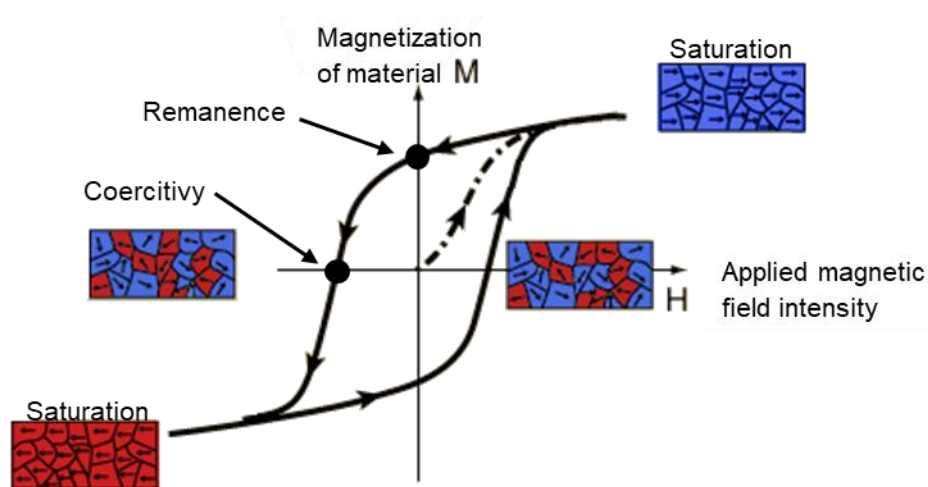


Figure 1.6. Sketch of typical M-H curve (hysteresis loop) with the indication of the most relevant points during the field loop together with the schematic visualization of the magnetic domain configuration: "magnetization saturation" M_s , that is maximum value reached by the magnetization; "remanence magnetization" M_r , i.e. magnetization at zero field; coercive field H_c , value of the field at zero magnetization.

2. Experimental techniques

For the realization of this work, it was necessary to use different techniques for the preparation of nanostructures as well as for their systematic characterization. Therefore, I will first describe the instrumentation exploited for the fabrication of the samples, and then the techniques exploited for the magnetic characterization.

The growth and magnetic characterization of the samples has been performed in the Nanomagnetism laboratories in IMDEA Nanoscience [1].

2.1. The growth chambers

The laboratory of epitaxial growth has a complex Ultra-High-Vacuum (UHV) system for the growth, by sputtering and molecular beam epitaxy (MBE), and the analysis of the surface/interface chemical, electronic and structural properties by X-ray and Ultra-Violet photoemission spectroscopy (XPS-UPS) and low electron energy diffraction (LEED). To note that the two UHV chambers (growth and analysis, see Fig. 2.1) are connected in UHV avoiding in this way any ambient contamination during the growth and analysis procedures.

The growth part of the system is composed by two vacuum chambers, one dedicated to the molecular beam evaporation (MBE) of organic and inorganic materials (with base pressure of $\sim 10^{-10}$ mbar, on the left in Fig. 2.1), and the other dedicated to the sputtering deposition of metals (with base pressure of $\sim 10^{-8}$ mbar).

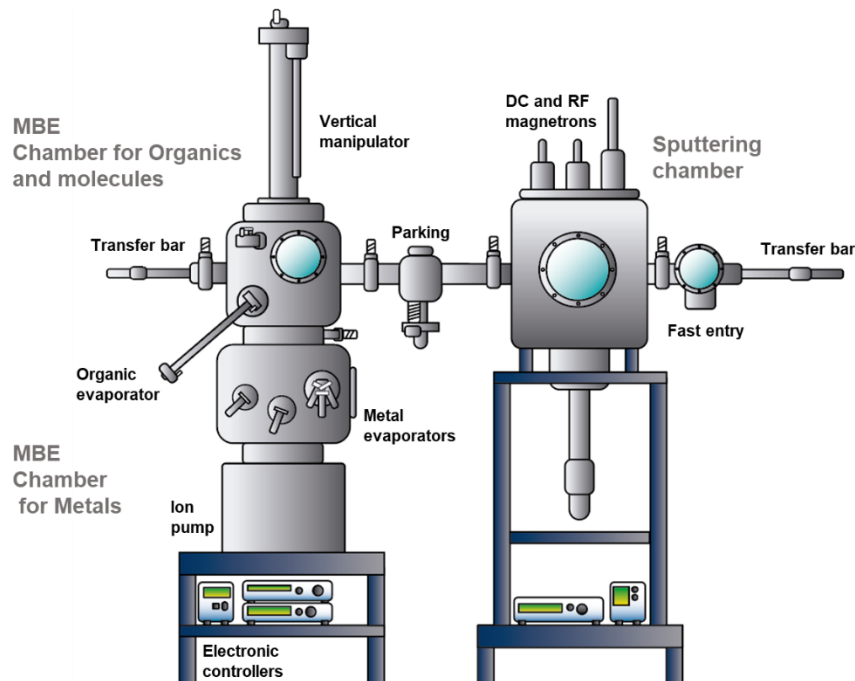


Figure 2.1. Schematic configuration of the growth system composed by the MBE chamber equipped with various e-beam evaporators and Knudsen cells (on the left) and the sputtering chamber hosting 5 dc and 1 rf magnetrons (on the right). The two chambers are in-situ connected through a smaller chamber used to store in UHV condition samples (“parking”).

2.1.1 Sputtering chamber

The sputtering technique is largely used for both investigation purposes and industrial production. This is due to its versatility (very large range of materials can be grown using this technique) and scalability allowing fast growth (due to the high rate of deposition) even over very large surfaces ($\sim\text{in}^2$). In addition, due to the high deposition rate, it is possible to grow complex structures with the thicknesses ranging from sub-nm size to several microns.

The mechanism of the sputtering technique is quite simple (see sketch in Fig. 2.2). It is based on the ionic bombardment of the material (namely, target placed in the electric cathode) that we want to deposit on a specific substrate (usually placed in front of the target, electric anode).

The principle of the sputtering process can be seen in Fig. 2.2. The target is placed at the cathode. An inert gas such as Ar is inserted between the electrodes. Oxygen (O_2) is often mixed with Ar during the deposition of oxides. When an electric field in DC or at radiofrequency (RF) (typically 13,56MHz) is applied across the electrodes, electrons are emitted from the cathode. The electrons, being accelerated by the field, collide with the gas atoms, generating ions and yet more electrons (secondary electrons). The Ar^+ ions are accelerated towards the cathode and sputter the material that constitutes the target. The trajectories of the electrons are bent by a specifically designed magnetic field created by a special configuration of permanent magnets placed in the magnetron (magnetron sputtering), leading to a certain degree of confinement of electrons around the cathode (target) surface. This effectively increases the probability of ionization of the gas, permitting a higher deposition rate, usually in the range $10^{-2} - 10$ nm/sec also depending on the target material. To note that the magnetrons must be water-cooled to avoid that the temperature of the cathode (and therefore of the permanent magnets) increases more than the Curie temperature of the magnets. The rate at which we can grow depends on the type of material we employ (each material has a different *sputtering yield*), and the power that the magnetron supplies.

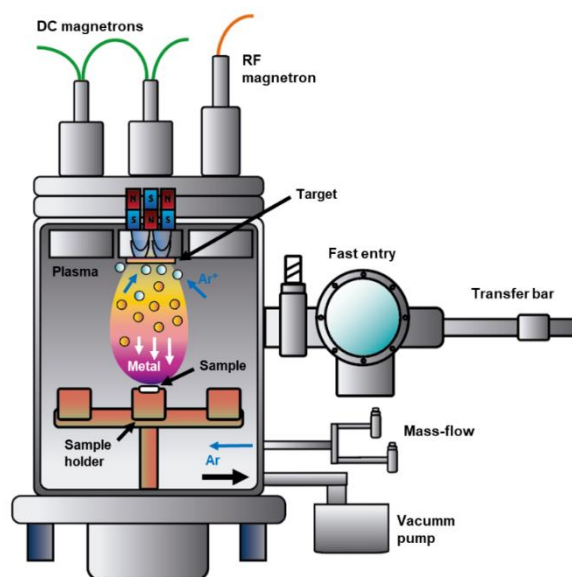


Figure 2.2. Schematic of sputtering chamber. The system is equipped with a “fast entry” chamber that allows for the insertion of the sample without breaking the vacuum condition of the main chamber.

The sputtering chamber employed in this work is equipped with 5 DC and one RF magnetrons. It allows the growth of multi-layered samples with a wide range of combinations of different materials. In the last chapter, I will detail the growth condition and the composition of the stacks investigated.

2.2. Vectorial-Kerr magnetometry

A linearly polarized beam of light reflected by a magnetized surface in the direction of propagation of the incident beam may change its polarization. This effect is known as Kerr effect, from its discoverer namely John Kerr [14]. The analogous effect for transmitted light takes the name of Faraday effect (from Michael Faraday [15]). The magneto-optical technique that exploits the Kerr effect is called Magneto-Optical Kerr effect (MOKE) and is a very sensitive and powerful technique to study the magnetization reversal pathways as well as the magnetic anisotropy symmetry of thin films with thickness ranging from sub-nm to tens of nm. Due to the wavelength of the light source used (from UV to IR, generally IR light is used) the penetration depth and hence the probing thickness of the sample is of the order of several tens of nm over an illumination area (i.e. sample surface area) ranging from μm^2 to mm^2 . To note that the sample area that can be investigated is only limited by the optical capability to reduce the beam spot.

Briefly, a MOKE measurement consists in measuring the rotation of the polarization of the reflected light, from which we deduce the magnetization state of the sample as function of an externally applied magnetic field [16].

Three MOKE configurations are normally employed, classified by the set-up geometry, i.e. the relationship between the direction of the light, the plane of the sample surface and the direction of the magnetic field (and consequently the direction of magnetization), as schematically shown in Fig 2.3.

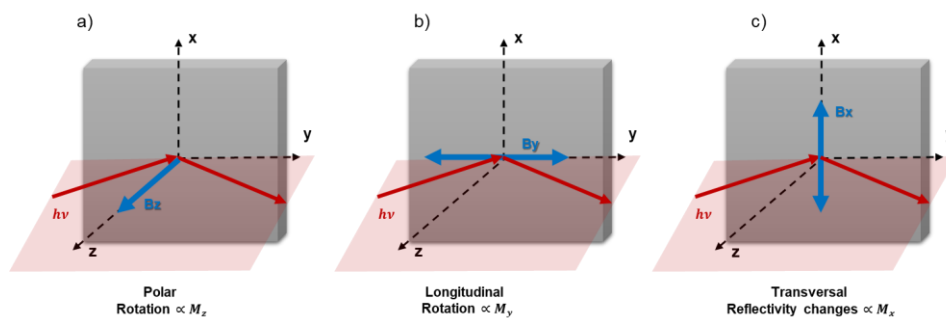


Figure 2.3. Standard MOKE geometries. a) Polar: the magnetic field \mathbf{B} is applied along the sample surface normal and within the plane formed by the incident/reflected beam. In this geometry, the Kerr rotation is sensitive to the magnetization component that lies in the plane formed by the sample normal and the incident/reflected light, i.e. M_z . b) Longitudinal: the magnetic field \mathbf{B} is applied parallel the sample surface and the Kerr rotation is sensitive to the magnetization component that lies in the sample surface and parallel to the external field, i.e. M_y . c) Transversal: the magnetic field \mathbf{B} is applied parallel but orthogonal to the plane formed by the sample surface normal direction and the incident/reflected beam. In this geometry, the Kerr rotation is proportional to the component of the magnetization parallel to the field, i.e. B_x . To note that the Polar geometry is used for sample with perpendicular magnetic anisotropy, whereas the Longitudinal and Transversal are employed typically for samples whose anisotropy is in-plane.

As illustrated in Fig. 2.3, in a first-order approximation, the longitudinal and polar MOKE geometries provide information about the magnetization components within the reflection plane (m_x and m_z , respectively) by measuring their corresponding polarization rotations [17][18]. Changes in reflectivity are measured in transversal geometry (m_y), perpendicular to the reflection plane. Usually, the polar Kerr signal is one order of magnitude greater than the longitudinal signal [17][18]. We can have a complete vectorial study on the magnetization making use of the three configurations.

Our experimental setup

If we center on the optical part of the system, this consist of a circular randomly polarized He-Ne laser ($5mW$, $\lambda= 632\text{ nm}$), a polarizer (s or p polarization choice), a lens that focuses the beam on the sample surface, a new focus-lens that focuses the beam again on a $\lambda/2$ -retarder that rotates the polarization of the reflected beam and a Wollaston-prism that split the beam into two separate beams. Finally, the intensities of the two waves are measured by two photodiodes [17][18], as it is illustrated in Fig. 2.4.

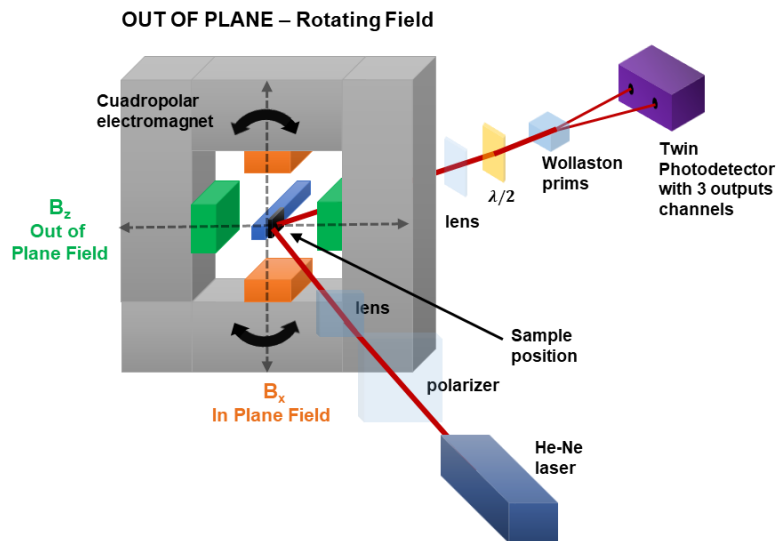


Figure 2.4. Scheme of the v -MOKE setup in Polar geometry.

The photodiodes, ending up with three outputs channels for the difference DC (ΔI), sum DC (ΣI_{DC}) and the sum AC (ΣI_{AC}) signals of the two orthogonal polarization components of the reflected beam). Lastly, these signals are read with a digital oscilloscope. In few words, the difference of the intensities (ΔI) is proportional to polarization rotations, while the alternating component of the sum of intensities (ΣI_{AC}) is proportional to reflectivity changes. The ΣI_{DC} is used to normalize the data. Both signals are measured at the same time, providing the determination of the two in-plane magnetization components simultaneously. For this reason, in a single measurement procedure it is possible to acquire the hysteresis data (transverse and longitudinal components) of a sample for the whole in-plane angular range. The noise is notably reduced by averaging several measurements taken with the same conditions.

2.3. KERR Microscopy

Kerr microscopy is a useful imaging tool for the characterization of magnetic structures, giving back relevant information about the nucleation, propagation of magnetic domain walls even is useful for estimate his density or mean size.

The light source used for our setup is a LED lamp. As illustrated in Fig. 2.5, when the light passes through the collector, it focuses the light to the iris of the aperture diaphragm [19][20]. Aperture diaphragm is crucial in Kerr microscopy setup because while in a normal microscope it controls the optical resolution and intensity of illumination, here we

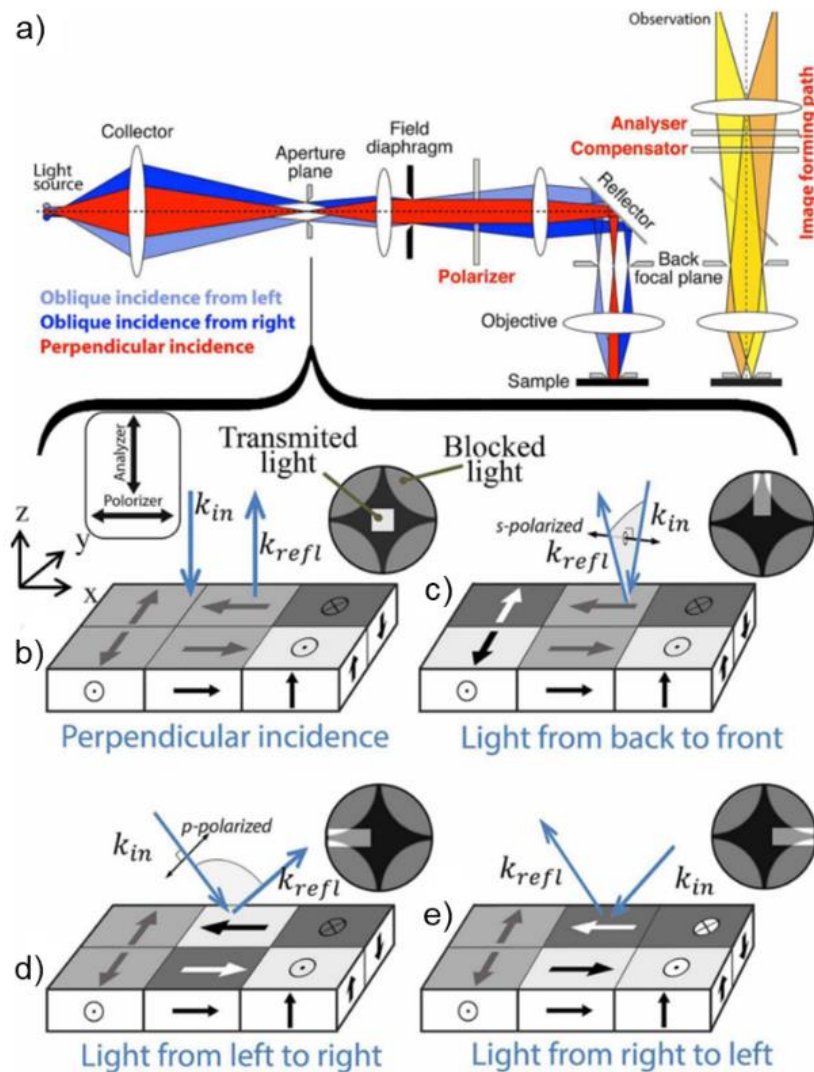


Figure 2.5. (a) Ray paths for illumination and image formation of a Kerr microscope with displaceable slit aperture, conventionally used for the adjustment of the sensitivity direction. Basic geometries of the Kerr contrast are illustrated: (b) polar contrast, (c) longitudinal with s-polarized light, (d) longitudinal in transverse direction with p-polarized light with direct and inverted contrast (e). Shown is a perspective view of vertically, horizontally and perpendicularly magnetized domains together with the conoscopic images in which the position of the slit aperture is indicated [20][21].

can control the angle of incidence by closing and opening the aperture diaphragm, and by moving it laterally, we can switch from longitudinal to transversal mode.

Then, a lens is used to focus the light to the back focal plane of the objective lens. Further, the light is collimated by the objective lens to illuminate the magnetic sample on the sample stage. The light illuminated on the sample is then reflected along with the changes due to the Kerr effect. The changes involved are polarization, intensity change and phase change depending on the type of MOKE that occurs in the magnetic sample. Subsequently, the polarizing beam splitter away from the illumination light path reflects the reflected light. Thus, the light together with the changes goes through the compensator and analyzer. The compensator used in the setup is a quarter wave plate. The analyzer translates the plane polarization change into an intensity change and the image is focused on the CCD sensor. To note that, due to the weak nature of the effect, the magneto-optical contrast is mainly achieved via signal and imaging post-processing. Therefore, it is essential to maximize the signal-to-noise ratio by appropriate optimization of the experimental set-up, measurement parameters and post-processing data-treatment technique (like to take the background and subtracting it or take images with averaging to try to reduce the noise). In addition, it is possible to study the samples not only in static regime but also as function of the magnetic field sweep rate (dynamics).

3. Results

In this chapter, the growth of polycrystalline stacks with perpendicular magnetic anisotropy and symmetric and asymmetric interfaces together with the magnetic characterization are presented.

Three types of structures were fabricated on the Ta(5nm)/SiO₂/Si(111) surface and then analyzed: *a*) Pt ($t_{\text{Pt-wedge}}$) / Co (t_{Co}) / Pt (5nm), *b*) Pt ($t_{\text{Pt-wedge}}$) / Co (t_{Co}) / Ta (5nm), and *c*) Pt (t_{Pt}) / Co ($t_{\text{Co-wedge}}$) / Pt (5nm). Structures *a*) and *b*) were employed to optimize the Pt thickness to achieve defined magnetic anisotropy of Co with fixed thickness. Structure *c*) was realized to study the magnetic field dependent magnetization hysteresis loops and the magnetic domain configurations as function of the FM Co thickness.

3.1. Growth process

The samples have been fabricated by DC magnetron sputtering onto 10x5 mm² commercial Silicon (Si) (111)-oriented substrates with 300 nm thick oxidized SiO₂ top-layer in the sputtering system (base pressure 8x10⁻⁸ mbar) as described in Chapter 2. The Si wafers were regularly cleaned by acetone and isopropanol in an ultrasound bath and dried with Nitrogen to remove organic contaminations. A first 5 nm thick Ta layer was deposited from polycrystalline commercial target in order to cap the SiO₂, favoring the (111) crystallographic orientation [21]. A partial Ar pressure of about 6.3x10⁻³ mbar was used to stabilize a homogenous plasma. The subsequent metallic layers, i.e. Pt, and Ta heavy metals (HM), and Co ferromagnetic (FM), were then sputtered from commercial targets and in the same partial pressure condition. The deposition rate for each material was measured before the growth by means of a quartz balance by tuning the density and material factor specific for each target.

As discussed in Chapter 1, the magnetic anisotropy depends strongly on the FM layer thickness and its crystallographic orientation. In ultra-thin FM films, in fact, the surface anisotropy term overcomes the volume anisotropy (see [Equation 3](#)), thus favoring a perpendicular alignment of the magnetization. Hence, it results of great relevance to optimize both HM buffer and FM thickness to define the desired overall magnetic properties of the stacks.

Three types of samples were fabricated onto the Ta(5nm)/SiO₂/Si(111) surfaces: *a*) Pt ($t_{\text{Pt-wedge}}$) / Co (t_{Co}) / Pt (5nm), *b*) Pt ($t_{\text{Pt-wedge}}$) / Co (t_{Co}) / Ta (5nm), and *c*) Pt (t_{Pt}) / Co ($t_{\text{Co-wedge}}$) / Pt (5nm). Samples *a*) and *b*) present a buffer Pt layer with different thickness (from 5 to 15 nm) over the surface (wedge) as illustrated in Fig. 3.1. These structures serve to optimize the magnetic properties of the entire stack. By fixing the optimal Pt thickness to 5 nm, we fabricated sample *c*) with Co wedge, i.e. varying its thickness from 0.8 to 1.8 nm, to study the spin reorientation transition (from perpendicular to in-plane magnetic anisotropy) and the overall magnetic properties.

The method employed to grow “flat” or “wedge” layer slightly changed. In both cases, the substrate and target are placed on in front of the other as shown in Fig. 2.2 (Ch. 2). In the case of the wedge samples, the position of the substrate was step-by-step moved

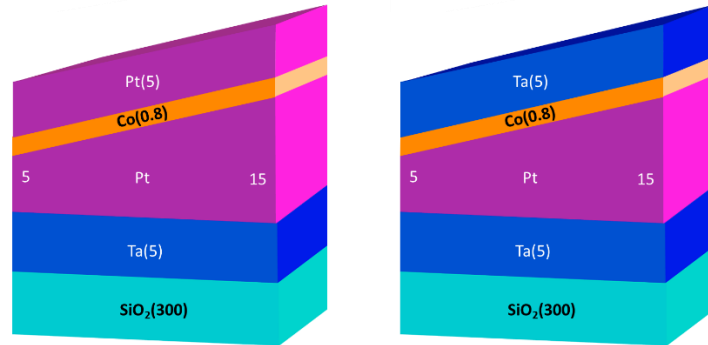


Figure 3.1. Schematic illustrations of the samples structures: on the left, the symmetric stack Pt/Co stack grown onto a Pt-wedge; on the right, the asymmetric stack Ta/Co stack grown onto a Pt-wedge.

away from the center of the plasma keeping constant the deposition rate to ensure homogeneity of the growth. Therefore, one side of the substrate surface presents larger thickness than the opposite side.

3.2. Structures a) Pt (t_{Pt} -wedge) / Co (t_{Co}) / Pt (5nm) and b) Pt (t_{Pt} -wedge) / Co (t_{Co}) / Ta (5nm)

The magnetic properties of the stacks were investigated by means of Polar Kerr Magnetometry described in Ch. 2. We have measured the perpendicular magnetization

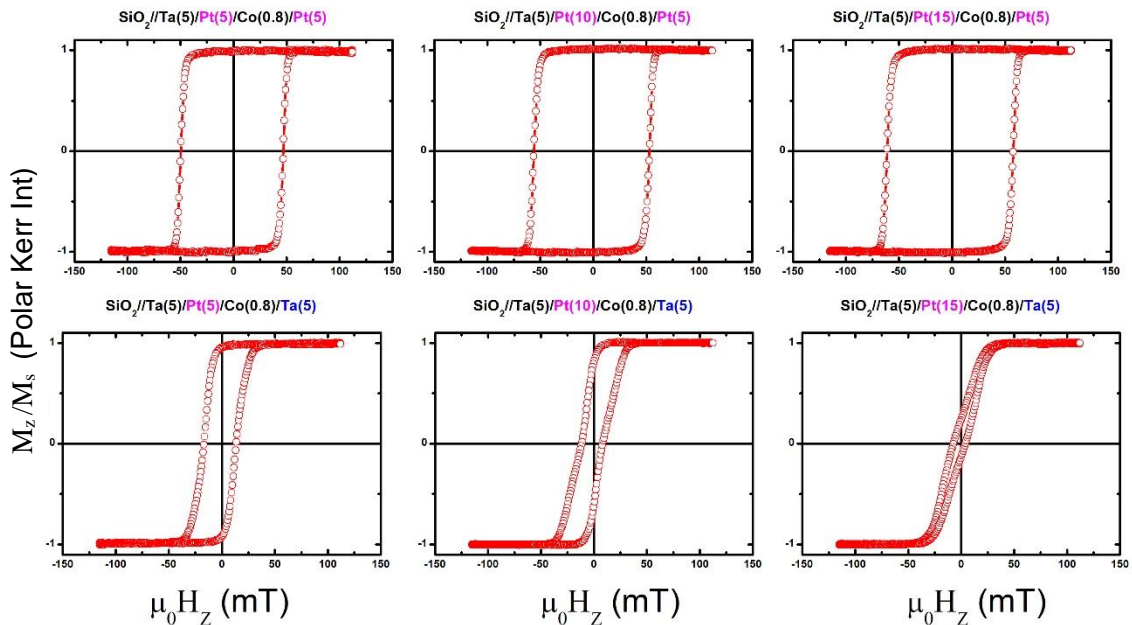


Figure 3.2. Polar Kerr hysteresis loops for selected Pt thicknesses of symmetric (top) and asymmetric (bottom) stacks. The loops are normalized to the saturation magnetization.

component as function of the external magnetic field in different area of the sample surface corresponding to different Pt thickness.

Figure (3.2) presents the hysteresis loops of magnetization normalized to the saturation M_z/M_s as function of the out-of-plane field $\mu_0 H_z$ by illuminating the sample in different area which correspond to different Pt thickness for the symmetric a) (top-graphs) and the asymmetric stack b) (bottom-graphs).

At first glance, we notice that the symmetric stack presents larger coercive field and a remanence almost 100% of saturation independently from the Pt thickness (top-graphs). The shape of the curves (abrupt transitions and fully remanence) indicates that the magnetization reversal proceeds by nucleation of magnetic domains and further domain walls (DW) propagation. In contrast, the M_z/M_s vs $\mu_0 H_z$ curves (bottom-graphs) display more rounded transitions and reduced magnetization remanence, and a strong dependence with the buffer thickness. Specifically, the curve acquired in the area corresponding to the larger Pt thickness, i.e. 15 nm (bottom right graph), present an almost fully reversible loop with a remanence of about 20% of M_s . These features suggest that for the asymmetric stack the spin reorientation transition occurs for smaller Pt thickness than for the symmetric stack. In fact, by computing the evolution of M_z^{rem}/M_s as function of the Pt buffer thickness (Fig. 3.3), we clearly notice that no changes in the remanence signals can be appreciated in the symmetric stack, whereas a drop of M_z^{rem}/M_s is observed in the asymmetric stack. Such smooth drop indicates clearly a spin reorientation transition from perpendicular to in-plane magnetic anisotropy at around 11 nm.

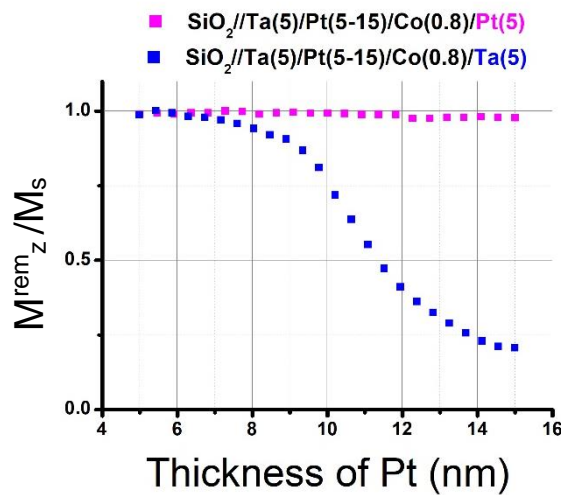


Figure 3.3. Remanence magnetization normalized to the saturation magnetization M_z^{rem}/M_s as function of the Pt thickness for the symmetric (pink dots) and asymmetric stacks (blue dots).

Even though in this work we focus on the symmetric stack, in which we have observed no relevant changes with Pt buffer, we have chosen as optimal buffer thickness 5 nm since it ensures better magnetic properties also for the asymmetric stacks that will be object of our research in the near future giving rise to a net (non-zero) DMI.

3.3. Structure c) Pt (t_{Pt}) / Co (t_{Co} -wedge) / Pt (5nm)

Once optimized and therefore set the buffer thickness to 5 nm of Pt, we investigate the magnetic properties of symmetric stack as function of the FM Co thickness ranging from 0.8 nm to 1.8 nm. This study will provide relevant information about the magnetization reversal mechanisms as well as the spin reorientation transition from out of plane to in plane magnetic anisotropy. The sketch of the structure is presented in Fig. 3.4.

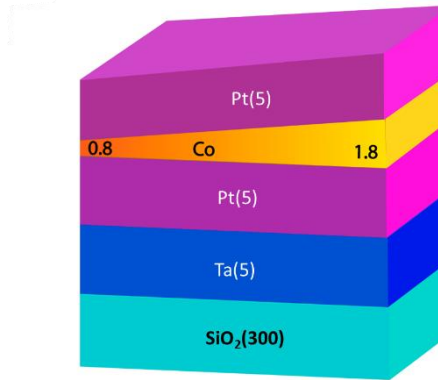


Figure 3.4. Schematic illustration of the sample structure: Pt (5nm) / Co (t_{Co} -wedge) / Pt (5nm).

Figure (3.5) presents selected hysteresis loops of magnetization normalized to the saturation M_z/M_s as function of the out-of-plane field $\mu_0 H_z$ by illuminating the sample in different area, which correspond to different Co thickness.

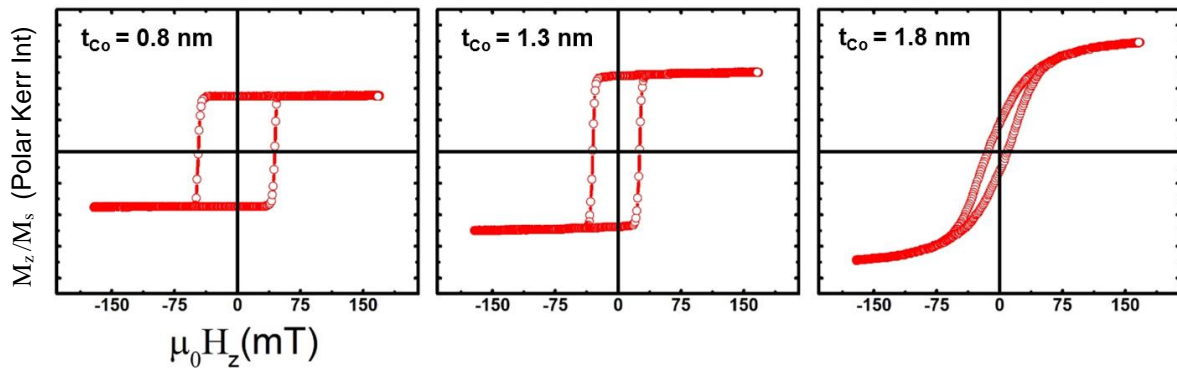


Figure 3.5 Polar Kerr hysteresis loops of Pt (5nm) / Co (t_{Co} -wedge) / Pt (5nm) with t_{Co} =0.8, 1.3 and 1.8 nm.

By inspecting the hysteresis loops, we notice that up to 1.4 nm of Co, the perpendicular hysteresis loop shows sharp transitions, large coercive fields and fully remanent state. As the Co thickness increases, more rounded transitions accompanied by smaller coercive fields and lower remanence magnetization are observed (Figure 3.5). This indicates a progressive decrease of the magnetic anisotropy with increasing Co thickness, which is confirmed by the evolution of the remanence magnetization (M_z^{rem}) normalized to the saturation magnetization (M_s). In fact, by computing the evolution of M_z^{rem}/M_s as function of the FM thickness as shown in Fig. 3.6, we clearly notice a reduction of the normalized remanence magnetization starting from 1.1 nm of Co. This proves that the magnetization points essentially out-of-plane up to 1.4 nm of Co [22].

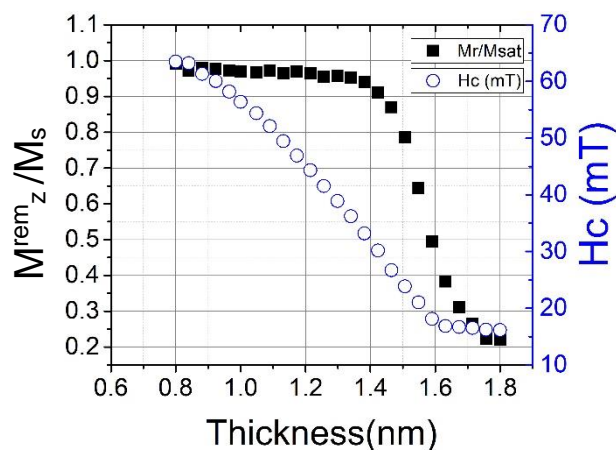


Figure 3.6 Remanence magnetization normalized to the saturation magnetization M^{rem_z}/M_s (black dots) and coercive field $\mu_0 H_c$ (blue circles) as function of the Co thickness.

To note that this value for the spin reorientation corresponds to what found in a symmetric structure with 5 nm Pt / 5 nm Ta buffer. Different layer sequence may present distinct Co thickness for the spin reorientation. Consequently, the coercive field smoothly decreases as the Co thickness increases (blue circles in Figure).

To symmetry of the magnetic anisotropy for two selected Co thickness has been investigated by performing an angular study of the M_z component of the magnetization as function of the intensity and direction of the external magnetic field by means of polar Kerr magnetometry. The magnetic field was varied from the perpendicular to the parallel to sample surface direction (by using a vectorial magnet). To note that $angle=0^\circ$ is taken for $H //$ to the normal to the sample surface. In this notation, the field direction parallel to the sample surface is hence $angle=90^\circ$.

The simplest information that can be extracted from the angular evolution is the anisotropy directions, determined by the magnetic symmetry of the system. This can be done easily by plotting the normalized remanence values of the magnetization as function of α_H (Figure 3.7 (left)). The magnetization component display a pronounced oscillation with periodicity of 180° for both thicknesses. The normalized remanence follows a $|\cos^2 \alpha_H|$ law dependence [23][24]. The polar plot (Figure 3.7 (right)) of M^{rem_z} display “two-lobes” shapes. All these features confirm a well-defined uniaxial perpendicular magnetic anisotropy behavior of the film.

In left part of the graph we have represented the transition fields, which correspond to the magnetic field for which the transitions occur required to compensate the magnetization along the field direction and to the effective anisotropy of the system. The pinning model reproduce the experimental data close to the anisotropy direction, i.e. magnetization easy axis (e.a.), where the reversal is dominated by irreversible process (nucleation and further propagation of magnetic domains). Nevertheless, the Stoner Wohlfarth (SW) model [25] only reproduces the angular evolution around the magnetization hard axis (h.a.) directions [17], i.e. perpendicular to the anisotropy direction, where reversible transitions corresponding to magnetization rotation mechanism are more relevant during the reversal. Unfortunately, due to the experimental limitation (maximum magnetic field provided by the vectorial electromagnet is about

250mT) we can not fully saturate the sample along the h.a in order to experimentally measure the anisotropy field. However, we estimated the anisotropy field by fitting the transition field with $H_t = a + b/\cos(\alpha_H)$. [24]

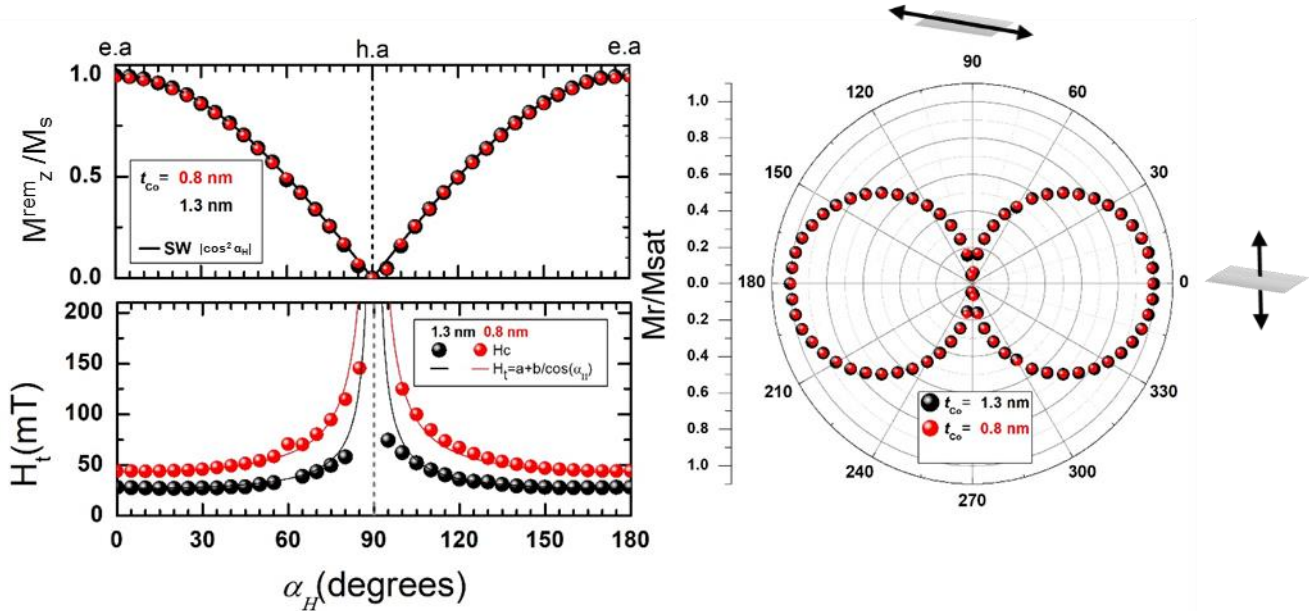


Figure 3.7 Remanence, transitions fields and magnetic symmetry of stacks with 0.8 nm and 1.3 nm thick Co layer: (top-left) Angular dependence of the normalized to saturation remanence magnetization; (right) Polar plot representation of the angular dependence of the normalized to saturation remanence magnetization clearly visualizing the perpendicular uniaxial magnetic anisotropy; (bottom-left) Angular dependence of the transition.

MOKE microscopy

The different magnetization reversal mechanisms highlighted by the magnetic field dependent hysteresis loops also effects the magnetic domains nucleation, propagation and size. By resorting to Polar MOKE microscopy (by using the set-up described in Ch. 2) we have imaged the magnetic surface after demagnetizing the sample in the perpendicular direction and as function of perpendicular magnetic field.

The measurements consisted in first demagnetized the sample by subjecting the stack to fast ac magnetic field reducing progressively the maximum field intensity. The sample resulted hence with 50% of the total domains pointing out up and 50% pointing down. After the demagnetization process, we have acquired microscopic images in the remanence state. This ensures to have high magnetic contrast that cannot be achieved in the region with 1.5 nm thick Co with lower anisotropy and dominated by rotative processes (the images display a gradual change of grey contrast).

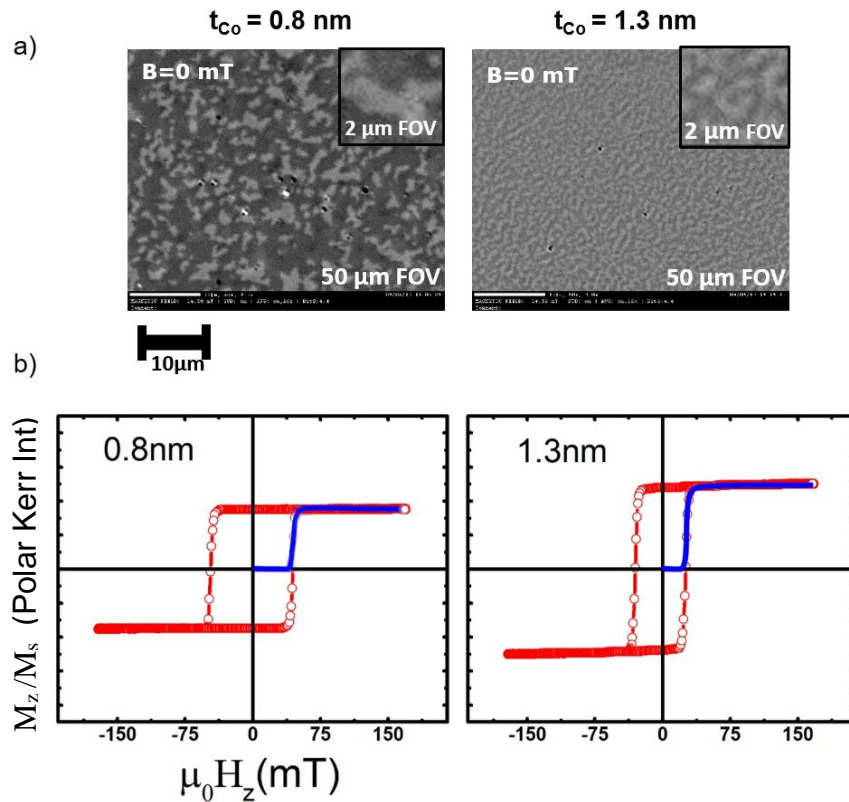


Figure 3.8 a) Selected polar MOKE microscopies for 0.8 nm (left) and 1.3 nm thick Co sample. b) Corresponding polar magnetization vs. field loops for 0.8 nm (left) and 1.3 nm thick Co sample.

The samples were measured in 5 areas with different Co thickness. By inspecting the Kerr microscopies we notice that the 0.8 nm thick Co region presents magnetic domains almost 3 order of magnitude larger than the ones obtained in the 1.3 nm thick Co region. The average domains size is related to the reduction of demagnetizing field as the Co thickness decreases [26]. To note that the resolution limit of the Kerr microscope is about $1 \mu\text{m}$.

Starting from this remanence magnetization state, we have changed the magnetic field perpendicular to the sample surface and acquired Kerr images for different field value. This is shown in Fig. 3.9. We hence notice that the density of magnetic domains increases in the region corresponding to larger Co thickness. We estimated the speed of propagation of the domains from subsequent images acquired after successive magnetic field pulses, finding that domains are faster in the thinner Co region [1][13][22].

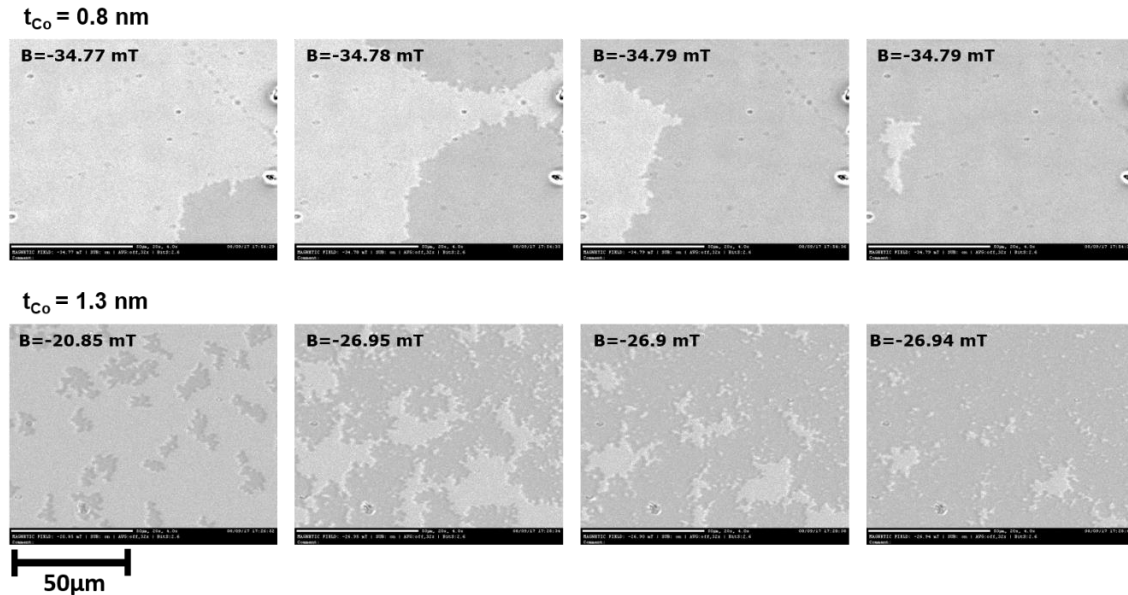


Figure 3.9 Kerr microscopies acquired in two distinct regions of the sample corresponding to 0.8 nm (top) and 1.3 nm (bottom) thick Co layer.

4. Conclusions

In this work, we have studied the fabrication by a dc sputtering deposition technique of heavy metal/ferromagnetic multilayers of interest in Spintronics and Spin-Orbitronics. We have investigated in details the magnetization reversal pathways, the magnetic anisotropy symmetry and imaged the magnetic domain structures by using different experimental techniques based on Kerr effect.

In particular, we have investigated the influence of the buffer Pt layer thickness on the overall magnetic properties of symmetric and asymmetric heavy-metal(1)/ferromagnet/heavy-metal(2) stack by fabricating samples with a buffer wedge Pt layer. We have then studied the effects of the ferromagnetic Co layer thickness by preparing sample with Co wedge. In both structures, we have discussed on the magnetization reversal, spin reorientation transition and magnetic anisotropy symmetry as well as on the magnetic domain nucleation and propagation.

These systems are at the basic constituent of the next generation magnetic devices based on smaller, faster and lower consumptive magnetic objects named magnetic skyrmions. This work has served as starting point for the realization of high quality complex structures with tuned magnetic anisotropy and tailored Dzyaloshinskii-Moriya interaction.

5. Acknowledgements

I would like to thank the group of Spin-Orbitronics at IMDEA Nanoscience Dr. Paolo Perna, Dr. Julio Camarero, Dr. Fernando Ajejas, Dr. Rubén Guerrero, Dr. Alberto Anadón, Dr. José Luis Fernández Cuñado, Dr. Javier Pedrosa, José Manuel Díez, Pablo Olleros, Leticia de Melo as well as Dr. Cristina Navio, Dr. Miguel Ángel Niño, Javier Rial, Melek Villanueva, for all the support during the experiments and discussion of the results. This work couldn't possible without their help.

6. References

- [1] F. Ajejas, "Symmetry breaking effects in spin(orbit)tronic systems", Universidad Autónoma de Madrid – IMDEA Nanociencia, (2017).
- [2] Fert; K. Bouzehouane; A. Barthelemy; M. Bibes & V. Cros. "Spin-orbitronics , a new direction for spintronics", 1 (2014).
- [3] A. Soumyanarayanan; N. Reyren; A. Fert & C. Panagopoulos, "Emergent phenomena induced by spin-orbit coupling at surfaces and interfaces". *Nature*, 539(7630), 509–517 (2016).
- [4] A. Fert; V. Cros; J. Sampaio. "Skyrmions on the track". *Nat. Nanotech*, 8, 152–156 (2013).
- [5] C. Kittel, "Physical Theory of Ferromagnetic Domains," *Rev. Mod. Phys.*, vol. 21, no. 4, pp. 541–583, (1949).
- [6] J.A.C. Bland & B. Heinrich, "Ultrathin magnetic structures; *Springer*, Berlín (1994).
- [7] J. Camarero, "Epitaxia de heteroestructuras magnéticas de baja dimensionalidad asistida por surfactantes", Universidad Autónoma de Madrid, (1999).
- [8] A. Fert; P.M. Levy, "Role of Anisotropic Exchange Interactions in Determining the Properties of Spin-Glasses". *Phys. Rev. Lett.* 1980, 44, 1538–1541.
- [9] J. Sampaio; V. Cros; S. Rohart; A. Thiaville; A. Fert, "Nucleation, stability and current-induced motion of isolated magnetic skyrmions in nanostructures." *Nat. Nanotech.* 2013, 8, 839–844.
- [10] O. Boulle; J. Vogel; H. Yang; S. Pizzini; D. de Souza Chaves; A. Locatelli; T.O, Menteş; A. Sala; L.D Buda-Prejbeanu; O.Klein et al.. "Room-temperature chiral magnetic skyrmions in ultrathin magnetic nanostructures". *Nat. Nanotech.* 11, 449 (2016).
- [11] D. Maccariello; W. Legrand; N. Reyren; K. Garcia; K. Bouzehouane; S. Collin; V. Cros; A. Fert, "Electrical detection of single magnetic skyrmions in metallic

- multilayers at room temperature". *Nat. Nanotech.* doi.org/10.1038/s41565-017-0044-4 (2018).
- [12] C. Moreau-Luchaire; C. Moutafis; N. Reyren; J. Sampaio; C.A.F. Vaz; N. Van Horne; K. Bouzehouane; K. Garcia; C. Deranlot; P. Warnicke et al. "Additive interfacial chiral interaction in multilayers for stabilization of small individual skyrmions at room temperature". *Nat. Nanotech.* 11, 444-448 (2016).
- [13] F. Ajejas; V. Křížáková; D. De Souza Chaves; J. Vogel; P. Perna, R. Guerrero, **A. Gudín**; J. Camarero & S. Pizzini, " Tuning domain Wall velocity with Dzyaloshinskii-Moriya interaction", *Applied Physics Letter*, 111(20), 202402 (2017).
- [14] J. Kerr, *Phil. Mag*, no. 3, p.339 (1877) & no.5, p.161 (1878).
- [15] M. Faraday, *Trans. Roy. Soc. London*, no. 5, p.592. (1846).
- [16] S.D Bader; E.R. Moog; P. Grünberg, *JMMM* 53, L295 (1986) Z.Q Qiu; S.D Bader, *JMMM* 200, 664 (1999).
- [17] E. Jiménez, et al., *Review of Scientific Instruments*, 85(5), 053904 (2014).
- [18] J.L.F. Cuñado; A. Bollero; T. Pérez-Castañeda; P. Perna; F. Ajejas; J. Pedrosa; **A. Gudín**... & J. Camarero, " Emergence of the Stoner-Wohlfarth astroid in thin films at dynamic regime", *Scientific report*, 7(1), 13474 (2017).
- [19] Z. Bin & H. Hujan, "Magneto-Optical Effect Microscopy Investigation on Permalloy Nanostructures", University of York, (2013).
- [20] V.I. Soldatov & R. Schäfer, "Selective sensitivity in Kerr microscopy", *Review of Scientific Instruments*, 88(7), 1-9 (2017).
- [21] N.H. Kim; D.S. Han; J. Cho; J.S. Kim; H.J. Swagten; C.Y. You, "Improvement of the interfacial Dzyaloshinskii-Moriya interaction by introducing a Ta buffer layer", *Applied Physics Letters*, 107(14), 142408 (2015).
- [22] F. Ajejas; **A. Gudín**; R. Guerrero, M.A. Niño; S. Pizzini; J. Vogel & J. Camarero, "Unravelling Dzyaloshinskii-Moriya interaction and chiral nature of Graphene/Cobalt interface", *arXiv preprint arXiv:1803.07443* (2018).
- [23] S. Chikazumi, "Physics of Ferromagnetism", *Oxford Science Publications*, Oxford, U.K (1997).
- [24] D. Givord; P. Tanaud & T. Viadieu, " Angular dependence of coercivity in sintered magnets", *Journal of magnetism and magnetic material*, 72(3), 247-252 (1988).
- [25] E.C. Stoner & E.P. Wohlfarth, "A mechanism of magnetic hysteresis in heterogeneous alloys", *Phil. Trans. R. Soc. Lond. A*, 240(826), 599-642. (1948).
- [26] B.D. Cullity; C.D. Graham, "Introduction to Magnetic Materials", 2nd Edition *Wiley* (1972).